Doppler Lidar Observations of a Downslope Windstorm

PAUL J. NEIMAN

Cooperative Institute for Research in the Environmental Sciences, University of Colorado/NOAA, Boulder, Colorado

R. M. HARDESTY, M. A. SHAPIRO AND R. E. CUPP

NOAA/ERL/Wave Propagation Laboratory, Boulder, Colorado

(Manuscript received 12 February 1988, in final form 5 May 1988)

ABSTRACT

During January and February 1987, the NOAA/WPL pulsed Doppler lidar was deployed in the foothills west of Boulder, Colorado, to study orographically induced flows over the Continental Divide. On 29 January 1987, the lidar, with its unique spatial and temporal data-gathering capabilities, documented a downslope windstorm affecting the Boulder area and the rest of the Front Range. The lidar recorded in detail 1) a low-level leeside wind maximum, 2) propagating wind gusts exhibiting two distinct periodicities, and 3) the eastern edge of a mountain wave feature where a jumplike flow reversal occurred. Such structures have not previously been observed with comparable detail by conventional in situ and remote sensing instruments. The observed phenomena were similar to results obtained from mountain-wave numerical models. The most notable of the structural similarities was between the observed and modeled wind gusts.

1. Introduction

People living on the leeside of large mountain ranges throughout the world are familiar with the effects that the mountains have on their local weather. The Front Range cities of the Colorado Rockies, especially Boulder, Colorado, are subject to strong mountain-induced windstorms, which on occasion produce significant structural damage (Lilly and Zipser 1972). A number of topographic and meteorological factors have an important role in making Boulder a prime location for severe downslope windstorms. For instance, the Continental Divide is, at this latitude, a well defined north–south oriented ridge with Boulder being near its closest point to the flat Plains to the east. This factor may result in accelerated wind flow east of the Divide when there is strong topographic wave response in the atmosphere above Boulder during strong west to northwest flow (Klemp and Lilly 1975). Strong flow across the Divide occurs during the cool season when a short-wave trough is superimposed on the climatological long-wave western North American ridge and is translating eastward into the long-wave eastern North American trough. Strong winds across the Divide also occur during anomalous periods of strongly zonal flow. According to Klemp and Lilly's (1975) linear, hydrostatic modeling studies, the topographic wave response and strong winds are enhanced by the ramp shape typical of the topography west of Boulder. Their modeling studies also showed that the location of the wind maximum was halfway between the Divide and the Plains. When nonlinear effects induced by mountain shape and height were included, the maximum shifted closer to the Plains (Klemp and Lilly 1978; Peltier and Clark 1979; Durran 1986). Its proximity to this area of predicted wind maximum makes Boulder quite vulnerable to strong downslope windstorms.

In January and February 1987, the National Oceanic and Atmospheric Administration/Wave Propagation Laboratory's (NOAA/WPL) pulsed Doppler lidar was used to investigate orographically induced flows, including downslope windstorms, east of the Continental Divide. From a site in the foothills ~7 km west of downtown Boulder, at an elevation of 1945 m MSL (Figs. 1 and 2), the lidar monitored fine-scale mountain flow features never observed in such detail by more conventional in situ and remote sensing instruments. The more interesting observations included 1) detailed velocity and backscatter structure of lee waves, 2) eddy-induced upslope flow reversal in the narrow foothills canyons, and 3) documentation of a downslope windstorm.

The 1986/87 winter along the Front Range was not characterized by frequent windstorms. However, one moderate windstorm occurred from Fort Collins, Colorado, to Lakewood, Colorado, early on 29 January 1987. Winds of up to 44 m s^{-1} commenced after 0430 UTC in Boulder and persisted for about 2.5 hours. The

Corresponding author address: Paul J. Neiman, CIRES, University of Colorado/NOAA, Boulder, CO 80309.

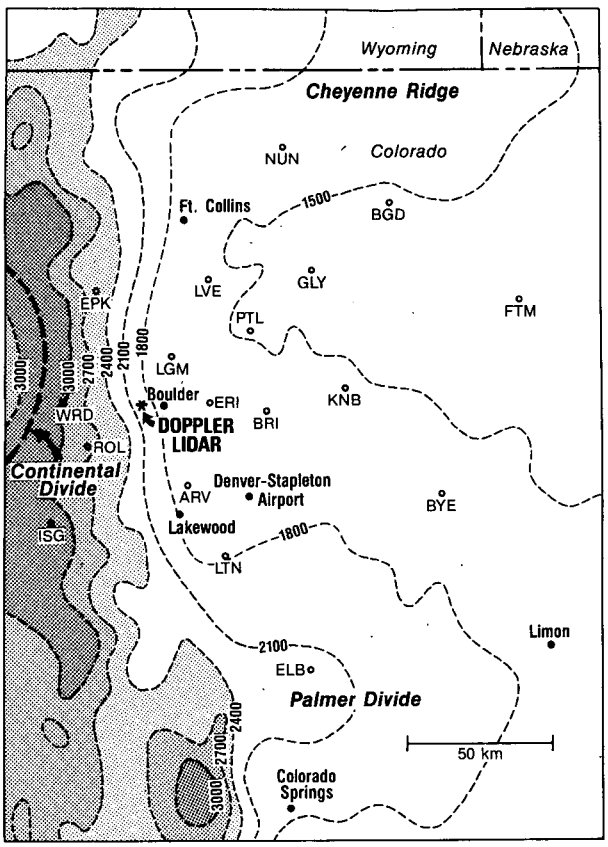

FIG. 1. The topography of northeastern Colorado. Elevation contours are in meters. The lidar is immediately west of Boulder.

Doppler lidar detected the abrupt onset and peak of the windstorm at the same time as the NOAA/Program for Regional Observing and Forecasting Services (PROFS) Mesonetwork (Pratte and Kaimal 1986). In addition, the lidar measured a low-level leeside wind maximum, and gustiness with two distinct periodicities near the time of the windstorm peak. This observed gust structure agreed with results of recent model studies by Clark and Farley (1984). Finally, the lidar observed a jumplike flow reversal characterized by a large horizontal velocity gradient over the eastern part of Boulder.

2. Synoptic overview of the 29 January windstorm

At 0000 UTC 29 January, the base of a 500 mb trough was entering extreme western Colorado (Fig. 3), and an associated surface cold front was approaching Denver (Fig. 4). Behind this front, very strong cold advection was occurring at 700 mb (Fig. 5). The precursors of the approaching cold front were first detected by WPL remote sensors at Denver–Stapleton Airport at ~2300 UTC 28 January. Cooling was observed in the lowest 1.5 km of the radiometric profiles (Fig. 6) in response to outflow generated by evaporative cooling from prefrontal convection along the Continental Divide to the west. This diabatic cooling in the mountains produced moist, negatively buoyant air, resulting in the downward motion detected by the Stapleton wind profiler vertical beam and a sharp increase in absolute humidity measured by the Stapleton radiometric profiler (not shown). The Stapleton profiler horizontal

FIG. 2. View looking east over Boulder from the lidar site atop a ridge 300 m above and 7 km west of the city. The terrain to the west of the site rises sharply to the Continental Divide (~4 km MSL) 30 km away.

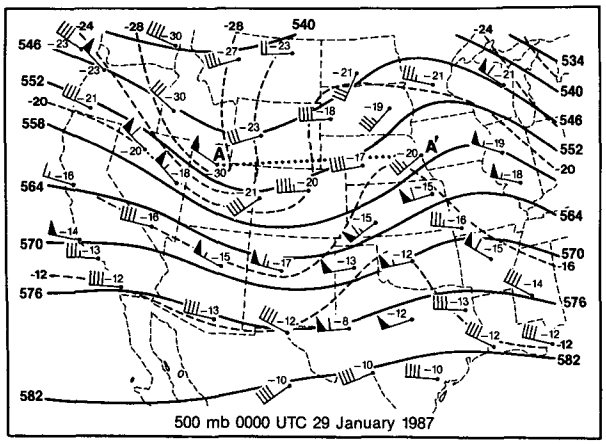

FIG. 3. The 500 mb height ($m \times 10$, solid lines) and temperature (°C, dashed lines) analyses at 0000 UTC 29 January 1987. The temperatures (°C) are printed in the upper left portion of the station plots. Wind vector flags: 25 m s^{-1}, barbs: 5 m s^{-1}, and half barbs: 2.5 m s^{-1}. Dotted line AA' is a projection line for the cross section in Fig. 8.

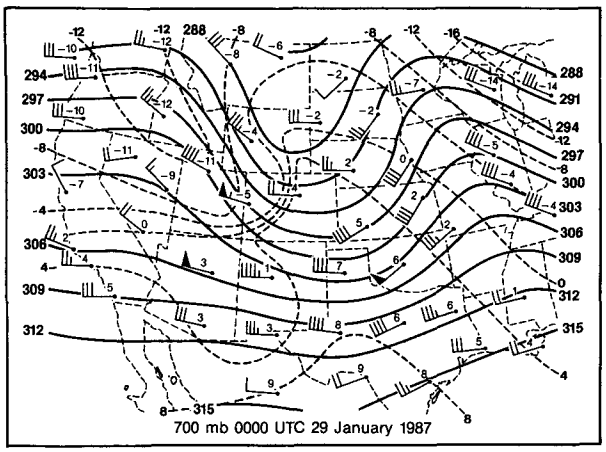

FIG. 5. The 700 mb height ($m \times 10$) and temperature (°C) analyses at 0000 UTC 29 January 1987. The temperatures (°C) are printed in the upper left portion of the station plots. Wind vectors are as described in Fig. 3.

wind measurements (Fig. 7) at the same time and in the lowest two to three gates showed a brief wind shift from southwest to stronger west-northwest in response to the outflow generated by the mountain convection and the downward transport of brisk west winds from mountain-top level. There was no pressure rise associated with the passage of the prefrontal boundary.

The front passed Boulder at ~0040 UTC 29 January when convection, cooling, and a surface wind shift from west to stronger northwest were observed. The front passed Stapleton Airport between 0108 and 0110 UTC when the shift to stronger northwest winds was observed (Fig. 7). A pressure jump was coincident with the frontal passage. The radiometric profiles detected the onset of an extended period of general cooling through a deep layer after frontal passage (Fig. 6).

At ~0450 UTC 29 January, the Stapleton wind profiler apparently observed the passage of the midtropospheric short-wave trough axis in the region between ~4.25 km above sea level (MSL) and the highest gate (5.5 km MSL) as west winds abruptly shifted to northwest (Fig. 7). The short-wave trough axis passed eastward from the Boulder foothills ~20 min earlier (0430 UTC), given a phase speed of 15 m s^{-1}. It was after 0430 UTC that the windstorm began at the lidar site. Only after the trough axis passage were the temperature (cold) advection and (anticyclonic) vorticity advection

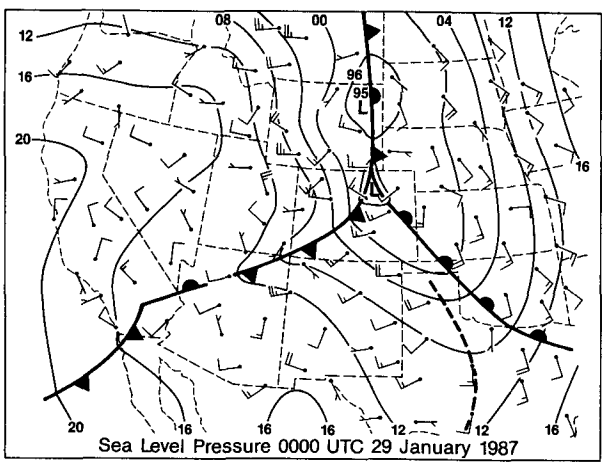

FIG. 4. Sea level pressure (mb) analysis at 0000 UTC 29 January 1987. Wind vectors are as described in Fig. 3.

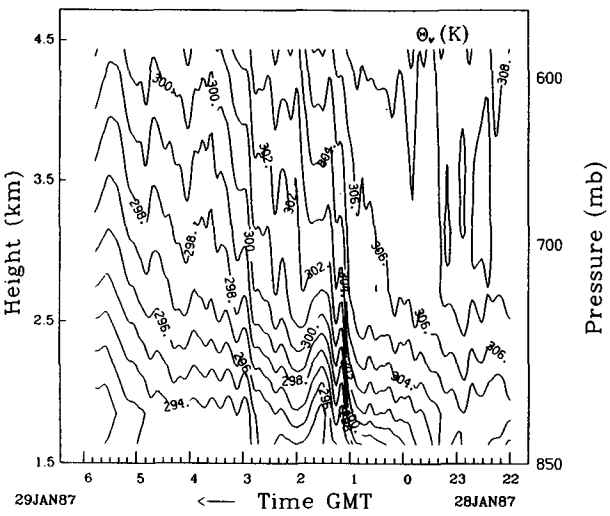

FIG. 6. Time–height section of filtered Stapleton radiometric Profiler virtual potential temperature, θ_v (K), from 2200 UTC 28 January 1987 to 0600 UTC 29 January 1987.

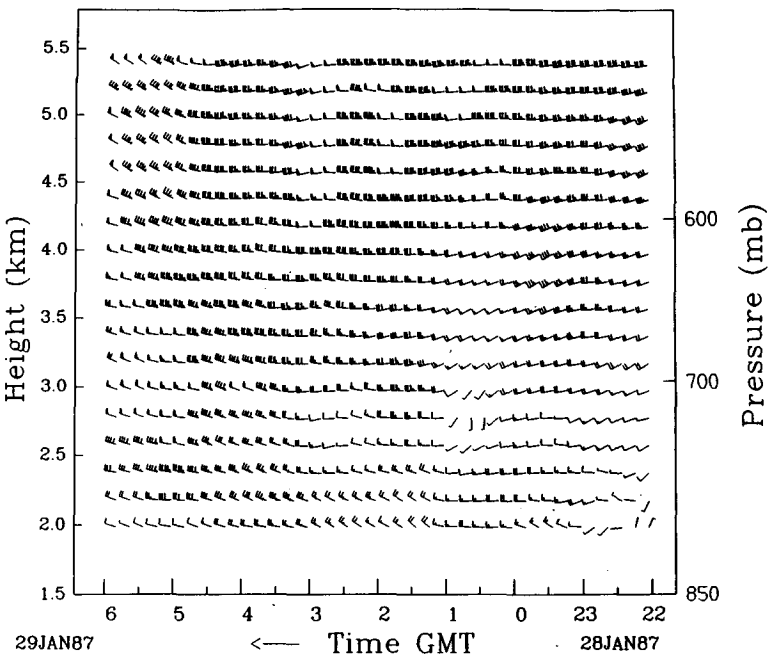

FIG. 7. Time–height section of filtered Stapleton wind profiler horizontal winds (m s^{-1}) from 2200 UTC 28 January 1987 to 0600 UTC 29 January 1987. Wind vectors are as described in Fig. 3.

both conducive to downward motion on the leeside of the Continental Divide (although no diagnostic vertical motion calculations were made in this study). Strong large-scale downward motion can, in the presence of strong westerly winds at mountain-top, enhance downslope windstorms. The Stapleton wind profiler vertical beam detected strong downward motion (approximately -1 m s^{-1}) throughout the depth of the profiles (up to 5.5 km) after the apparent midtropospheric trough axis passage. Although the observed downward motion may have been caused by the mountain wave (which produced the windstorm), the Profiler vertical beam measurements were consistent with subsidence west of the midtropospheric trough axis. During the windstorm, the west–east pressure gradient that was over western Colorado at 0000 UTC 29 January (Fig. 4) had translated eastward over the foothills, a potentially important development for the occurrence of windstorms (Lilly and Zipser 1972).

A west–east cross section of virtual potential temperature, θ_v, and wind vectors (Fig. 8, along the projection line AA' of Fig. 3) was constructed using five rawinsonde profiles and 15 surface observations (from Salt Lake City, Utah, to Omaha, Nebraska) at 0000 UTC 29 January. This analysis shows the front crossing the mountains. The stable frontal layer, with its associated vertical wind shear, sloped westward with increasing height, and exhibited deeper vertical extent to the west. The upper troposphere exhibited weaker ambient static stability than that of the frontal layer below and the stratosphere above. A weakly statically stable layer was found beneath the frontal zone over western Colorado and Utah. A deep adiabatic layer was observed along the Front Range, a consequence of turbulent mixing associated with prefrontal downslope conditions. A warm front in eastern Colorado, which had its origins as a lee trough earlier in the day (Fig. 4), defined the surface boundary between the deep, well-mixed lower troposphere along the Front Range and the western edge of the shallow, cold Canadian air mass to the east (Fig. 8).

A strong mountain-top stable layer, shown in Fig. 8, is believed to have an important role in producing downslope windstorms (Brinkman 1974; Durran 1986). The static stability structure observed in the cross section also appeared to favor strong leeside surface winds considering linear (Klemp and Lilly 1975) and nonlinear (Durran 1986) model simulation results. In comparison to previous Boulder windstorms, however, where recorded surface wind gusts have surpassed 50 m s^{-1}, the present storm was not unusually violent. Moist conditions upstream of the Continental Divide may have reduced the mountain wave response and strong leeside surface winds by effectively reducing the stability of the mountain-top stable layer (Durran and Klemp 1983).

3. Lidar time–height section analysis

The NOAA/WPL Doppler lidar has been used for a variety of studies of wind field structure (Post et al. 1978, 1981; Hardesty et al. 1983; Rothermel et al.

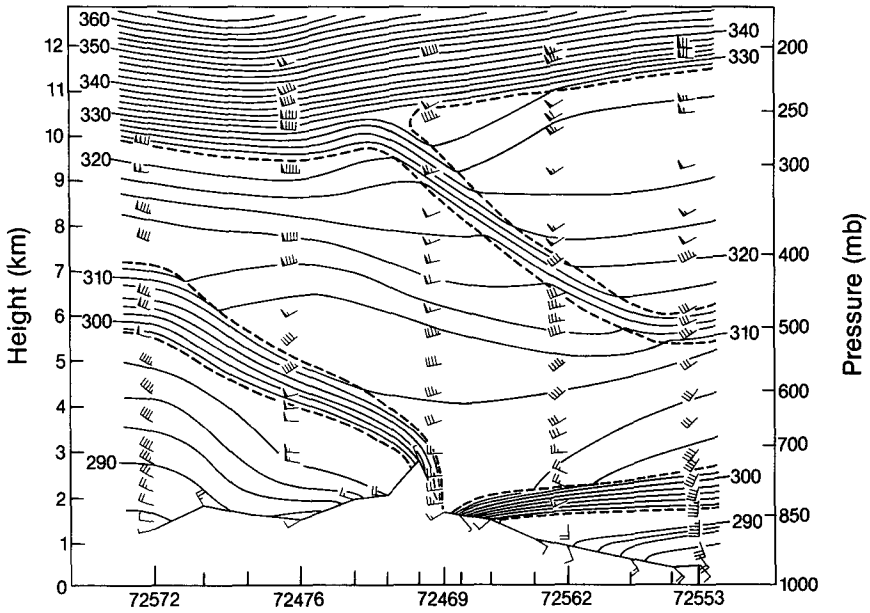

FIG. 8. Cross section of virtual potential temperature, θ_v (K, solid lines), and wind vectors at 0000 UTC 29 January 1987. National Weather Service rawinsonde data are from Salt Lake City, UT (72572), Grand Junction, CO (72476), Denver, CO (72469), North Platte, NE (72562), Omaha, NE (72553). Surface sites include, from west to east, Salt Lake City, Carbon, and Vernal in Utah, Grand Junction, Craig, Eagle, Winter Park, Denver, Byers, and Akron in Colorado, and Imperial, Grand Island, North Platte, Lincoln, and Omaha in Nebraska. Isentropes within dashed lines are stable layers, frontal layers, or the lower stratosphere. Wind vectors are as described in Fig. 3.

1985). During this study, in which the lidar observed a downslope windstorm, three different types of scans were analyzed. 1) Plan-position-indicator (PPI) scans measured circum-azimuthal slices of radial velocity at fixed elevation angles. Vertical profiles of horizontal wind were determined by applying the Velocity Azimuth Display (VAD) technique (Browning and Wexler 1968) to the PPI scans at fixed range gates. 2) West–east cross sections of radial velocity were obtained by range–height indicator (RHI) scans. 3) Range–time scans (which are discussed in more detail in section 4) measured spatial and temporal variability of the radial velocity along a one-dimensional beam directed due east from the lidar.

A time–height analysis of horizontal winds was prepared using six VAD lidar profiles taken between 0032 and 0738 UTC 29 January and two modified RHI cross sections taken 0529 and 0639 UTC. Each VAD profile was derived using a 10° elevation scan angle. At this angle, the closest range gate was 259 m AGL; a 300 m radial range gate interval corresponded to a 51 m resolution to the vertical wind profiles. Each RHI scan observation, which was composed of a field of radial velocities, was interpolated from polar coordinates to a Cartesian grid using an elliptical radius of influence (0.4 km in the horizontal and 0.2 km in the vertical), a median filter (5 m s^{-1} threshold, Velleman and Hoaglin 1981), and an inverse square weighting function. The grid spacing was 0.3 km in the horizontal and 0.1 km in the vertical. The horizontal wind component at each grid point was calculated assuming no vertical motion. By averaging the horizontal wind components at each level, and temporally interpolating the VAD wind directions to the RHI positions in time, the two RHI wind profiles were produced. Since the averaging domain at each level spanned a horizontal distance much larger than that of the embedded wavelengths, the error introduced by calculating the horizontal wind components in the upward motion portion of waves was balanced by the error in identical calculations in the downward motion portion of the same waves. The VAD and RHI vertical wind profiles were subjected to three passes of a temporal Hann filter to eliminate instrument-induced spurious data and remove natural atmospheric variability of $\leq$30 min periodicity while retaining the basic structure of the windstorm.

The time height analysis of horizontal winds (Fig. 9) during the onset of the windstorm ($\sim$0430 UTC) shows wind speeds increasing sharply from 20 to >36 m s^{-1} by $\sim$0545 UTC, when the peak of the storm occurred. After $\sim$0630 UTC, the winds slowly abated below 2.5 km. Unfortunately, the atmosphere above $\sim$3.5 km carried very little particulate matter as indicated by low backscatter intensity signals (not shown). As a result, the wind structure above this

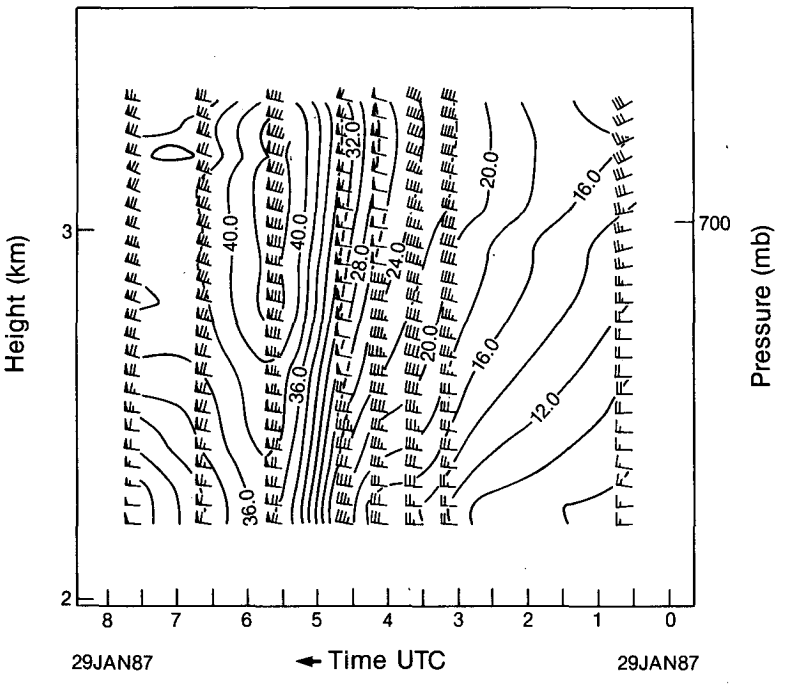

FIG. 9. Time-height section of Doppler lidar horizontal winds (m s^{-1}) from 0032 to 0738 UTC 29 January 1987. Wind vectors are as described in Fig. 3.

height could not be determined. An apparent low-level leeside wind maximum (above the surface) with winds of >42 m s^{-1} was observed near 700 mb at the peak of the event. This same feature was clearly detected by the 0529 UTC RHI scan (Fig. 10). A low-level leeside wind maximum was entered into the January 1972 windstorm analysis by Klemp and Lilly (1975) using surface pressure and wind information in and near the foothills, but was not directly measured. Linear and nonlinear windstorm model simulations have also depicted the leeside wind maximum (Klemp and Lilly 1975; Peltier and Clark 1979; Durran 1986). The present study is the first direct confirmation of the low-level leeside wind maximum. As a result of surface drag, the wind maximum was found above the surface. This observation differs from results of numerical model simulations that do not include surface drag and consequently show the leeside wind maximum at the surface. In Fig. 9, the strong winds started earlier at 700 mb than they did near the surface and may have been the result of surface drag.

Boulder's surface wind speed observations, averaged over 5 min intervals (Fig. 11), concur with the lidar time–height analysis. The strong winds in Boulder

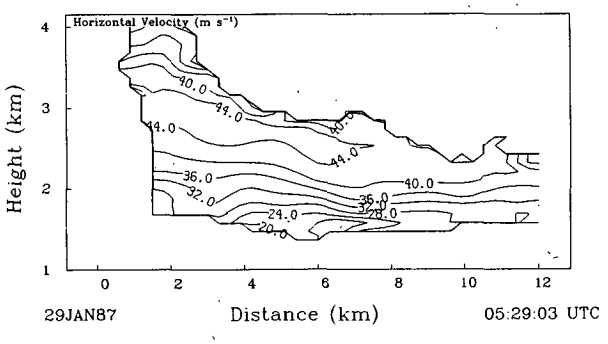

FIG. 10. Doppler lidar west-east range-height indicator scan of horizontal winds (m s^{-1}) at 0529 UTC 29 January 1987. The lidar is located at 0 km on the horizontal scale and 1.945 km on the vertical scale.

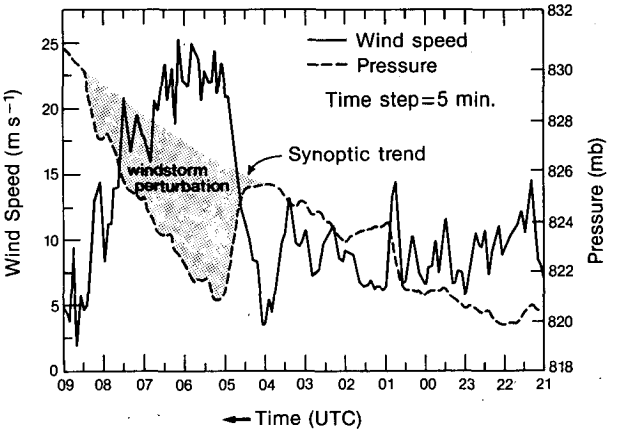

FIG. 11. PROFS Boulder mesonet time series of 5-min-averaged winds (m s^{-1}, solid lines) and pressure (mb, dashed lines) from 2100 UTC 28 to 0900 UTC 29 January 1987. The pressure perturbation caused by the windstorm is found within the stippled area.

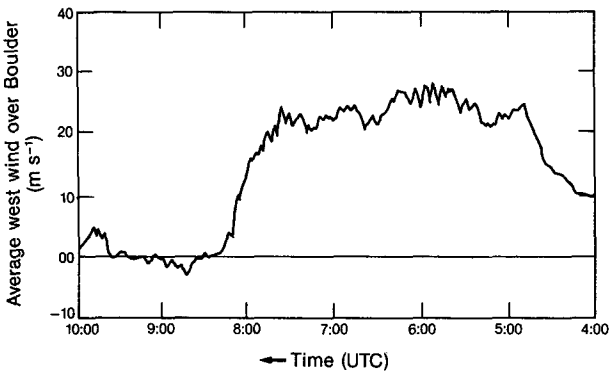

FIG. 12. Time series of the westerly wind component (m s^{-1}) measured by the WPL optical cross-beam wind sensor at 1 minute intervals from 0400 to 1000 UTC 29 January 1987.

commenced at ~0440 UTC when the wind speed exceeded 15 m s^{-1}. The maximum wind speed of 24.9 m s^{-1} averaged over 15 minutes occurred at 0545 UTC, and the event began its decline at ~0645 UTC. Wind gusts >30 m s^{-1} were observed in downtown Boulder starting at 0445 UTC; the peak gust of 39 m s^{-1} was at 0540 UTC. The WPL optical cross-beam wind sensor (described by Lawrence et al. 1972), located near the Boulder foothills during the storm, showed similar results (Fig. 12) with its north–south oriented beam measuring the westerly wind component. The 1-min-averaged winds exceeded 15 m s^{-1} at 0436 UTC, reached a maximum of 27.4 m s^{-1} at 0550 UTC, and began to weaken slightly at ~0630 UTC. Wind gusts were observed by the cross-beam sensor approximately every 3 to 4 minutes during the peak of the windstorm. The details of these gusts are discussed in section 4.

Boulder surface pressure averaged over 5 minutes, began to fall sharply at 0435 UTC, coincident with the start of the windstorm (Fig. 11). The pressure minimum occurred at 0515 UTC, while the windstorm was in progress. During the same period, the temperature showed a slow increase. On the basis of results from Lilly and Zipser (1972) and model results by Klemp and Lilly (1975), we suggest that the observed pressure falls during the windstorm may have been hydrostatically tied, at least in part, to the deformation of the isentropes within the mountain wave. The pressure falls may have also been tied to the strong winds, since pressure correlates negatively with wind speed through the Bernoulli equation. If two-dimensional flow is assumed, the 4.69 mb pressure fall observed during the windstorm corresponds (via the Bernoulli equation) to a windspeed of 30.6 m s^{-1}, which is consistent with observed wind speeds. A secondary pressure minimum was observed at 0550 UTC, superimposed upon a large-scale pressure rise, and coincided with the peak of the windstorm. After 0550 UTC, the temperature slowly dropped as the cold advection, which was hydrostatically linked to the pressure rise at this time, dominated the downslope warming.

4. Lidar range–time scan analysis

Two range–time scans were used in the present study. During the first scan (Fig. 13), the lidar was pointed eastward, with an elevation angle of −2° such that the optical beam intersected the ground at 12 km. The sampling rate was 0.2 Hz between 0550 and 0620 UTC. Perhaps the most intriguing observation from this windstorm was the propagation of wind gusts, with periods of ~4–5 minutes and ~14 minutes, away from the lidar (diagonal streaking in Fig. 13). Since the gusts maintained their identity in range and time, their pro-

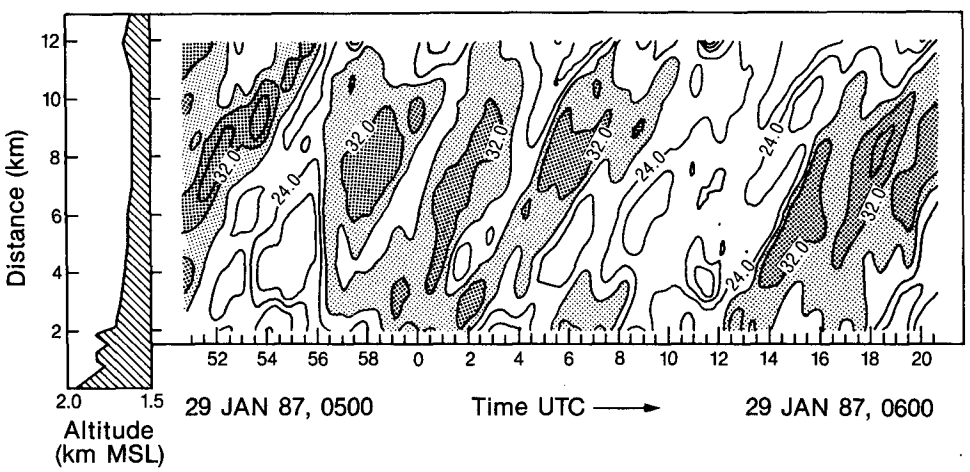

FIG. 13. Range–time display of lidar-measured radial velocities (m s^{-1}) during the period 0550 to 0620 UTC 29 January 1987. The lidar was pointed eastward with an elevation angle of −2°. The optical beam intersected the ground at 12 km range. The data within this scan were subjected to median and Lanczos filters (Velleman and Hoaglin 1981; Lanczos 1956) for display purposes only. Terrain along the lidar beam is shown to the left of the contoured lidar data.

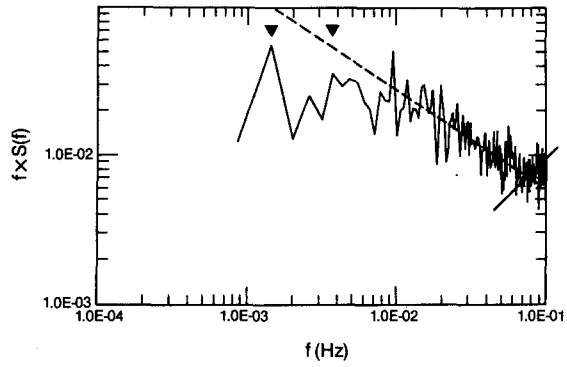

FIG. 14. Turbulence power spectrum ($m^2 s^{-2}$) compiled over all ranges from the velocity structure in Fig. 13. The two arrows point to the peaks corresponding to the ~4–5 and 14 min time scale oscillations observed in Fig. 13.

gression and strength across Boulder were easily monitored. The scan also monitored backscatter intensity signals. More backscatter was observed in the gusty regions, where large quantities of dust were being raised, and less backscatter was observed in the lull regions.

The turbulence power spectrum shown in Fig. 14 is a composite of the spectra calculated from all range gates of Fig. 13, and shows spectral peaks corresponding to the ~4–5 and ~14 min time scales. The ~14 min peak may lack statistical significance due to sparse data at this time scale, although the time series out to 9 km generally support such a peak. The spectra of all ranges were combined into a composite spectrum because the gusts and gust periods remained coherent in range and time. This compositing procedure was supported by the fact that along-beam profiles of horizontal velocity variance for discrete frequency windows showed little variation about the mean in the 12 km range. Note the good agreement at higher frequencies, f, with the $f^{-2/3}$ slope predicted by isotropic turbulence theory.

Through the Bernoulli equation, the wind speed and pressure are negatively correlated. Therefore, a pressure sensor located immediately east of and having a sampling rate identical to the lidar should theoretically yield a pressure spectrum from the time series that is the same as the lidar composite spectrum. Although it is difficult to accurately measure static pressure in a turbulent flow, we intend to employ pressure sensors in future windstorm studies so that we may be able to compare the wind and pressure spectra.

To obtain more precise information on the gust structure observed during the windstorm, the propagation and coherence of the observed wind gusts were calculated from a time-lagged correlation coefficient, $r(\tau, \rho)$, using the lidar-measured radial velocities in Fig. 13. The τ represents time lag between the time series being correlated, and ρ the separation distance in kilometers between the range-gate time series being correlated. In the cross-correlation analysis, the time series at each range gate was compared with the time series of the range gate $N\Delta R$ km farther downstream, where ΔR was the distance between range gates (0.3 km in this case), and the integer N was stepped between 0 and 33 range gates. For each of these comparisons, a time lag (TM s) was introduced, where T was the period between data points (2.5 s in this case), and the integer M was stepped between 0 and 348 points of the time series. A time-lagged correlation coefficient was calculated in the cross-correlation analysis for each ρ ($=N\Delta R$) and for each τ ($=TM$).

Figure 15 shows the correlation coefficient as a function of τ and ρ. The two broad correlation maxima are separated by 14–15 minutes, which corresponds to the larger-scale gust period observed in the range–time scan and composite spectrum. The fine-scale correlation maxima and minima are separated by ~4.0–4.5 minutes, which corresponds to the ~4–5 min gust period observed in the range–time scan and composite spectrum.

The spatial and temporal continuity of the correlation maxima and minima suggests that the gusts maintained their identity as they propagated away from the lidar. The primary correlation maximum (starting at $\tau = 0$, $\rho = 0$), which represents the initial propagation of the wind gusts from their original position in time and space, can be tracked out to 9 km before becoming indistinguishable (Fig. 16). Since the gust features were tracked for such a long distance (~9 km), it is likely that these gusts had a significant cross-wind (i.e., north–south) dimension. Otherwise, the gusts would have propagated out of the narrow lidar beam (~1 m) in a short period of time.

The propagation speed of the wind gusts can be determined by the slope of the correlation coefficient maxima and minima in Fig. 15. The gust propagation speed in this study was determined from the slope of the primary correlation maximum, which is representative of the average slope of the correlation features in Fig. 15. The primary correlation maximum was plotted as a function of τ and ρ out to 9 km (Fig. 17). When the least-squares linear regression technique was applied to the curve, the movement of the peak in τ for increasing ρ gave a gust phase speed of 27.5 m s^{-1}. This is nearly identical to the range–time scan ensemble radial velocity average of 27.2 m s^{-1} (Fig. 13), suggesting that the gusts were advected by the mean wind. The 27.5 m s^{-1} phase speed of the gusts translates to gust wavelengths of ~8 and 31 km corresponding to the two dominant gust periodicities. The optical cross-beam wind sensor recorded wind oscillations of about 3–4 minutes and a comparable 25.8 m s^{-1} average wind speed for the 30 min duration of the lidar range–time scan.

Recent windstorm numerical models have simulated gust structure similar to that observed by the lidar. Clark and Farley (1984) employed a third, along-mountain or cross-stream dimension to their two-dimensional anelastic, nonlinear, nonhydrostatic

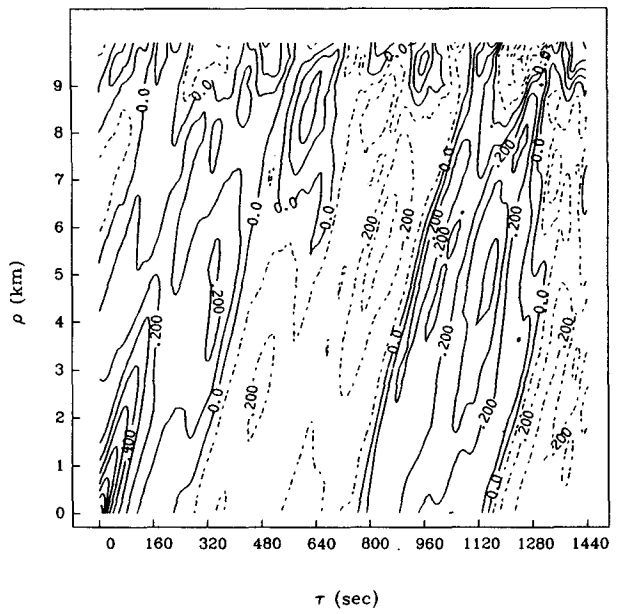

FIG. 15. Time-lagged correlation coefficient, $r(\tau, \rho)$, calculated from lidar-measured radial velocities in Fig. 13. Solid lines are positive; dashed lines are negative.

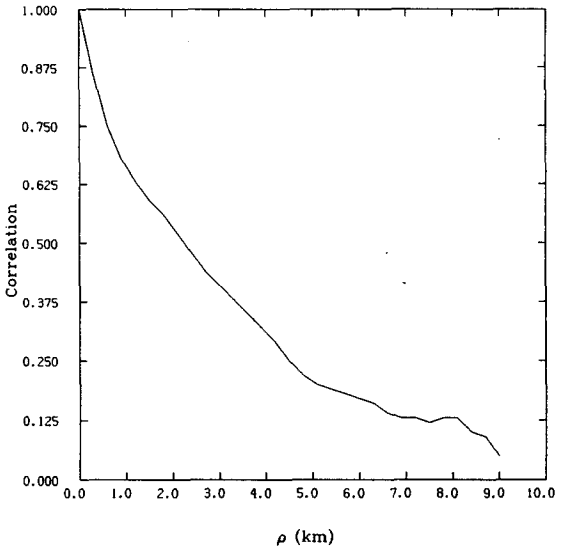

FIG. 16. Time-lagged correlation coefficient as a function of ρ for the primary correlation maximum in Fig. 15.

windstorm model. The major difference between the two- and three-dimensional models was found in the superadiabatic or critical regions, with only minor differences elsewhere. The most notable result of the three-dimensional simulation was the development of surface wind gusts in the favored windstorm region (the region where the two-dimensional model also predicted the highest surface winds) with a periodicity of 10–15 minutes. Clark and Farley speculated that the surface gustiness, which is commonly observed in downslope windstorms, originated in the superadiabatic region as turbulent eddies, and these eddies were transported to ground level along the western edge of the same convectively unstable region. The unstable region near the tropopause was considered to be the genesis region of severe turbulence often found in windstorms (Clark and Farley 1984). Clark and Farley suggested that the period of the wind gusts can be determined by the competition between mountain-wave buildup of a superadiabatic layer by forced gravity wave dynamics, and the wave breakdown from convective instability. Their model also showed that the surface gusts propagated downstream with time. The resemblance between model and observed wind gusts suggest that Clark and Farley's (1984) three-dimensional model may have captured essential aspects of the gustiness characteristic of windstorms. Furthermore, their speculation that an increase in spatial resolution would yield gustiness of less than 10–15 minutes may also be correct, since we observed a dominant small-time-scale periodicity of 4–5 minutes.

During the latter stages of the windstorm, a second range–time scan was produced (Fig. 18). The lidar pointed horizontally eastward, so that the optical beam never intersected the ground. The sampling rate was 0.4 Hz between 0708 and 0722 UTC. Coherent propagating gusts, with a 4–5 min periodicity common to the other range–time scan, were observed out to nearly 12 km (corresponding to a small terrain feature called Hoover Hill). The slope of these gusts, and hence their propagation speed, was essentially identical to the slope of the gusts in the first range–time scan. Between 0710 and 0715 UTC, a strong westerly wind speed gradient ($\sim$15 m s^{-1}/km) and flow reversal were observed east of Boulder beyond Hoover Hill. The strong westerly

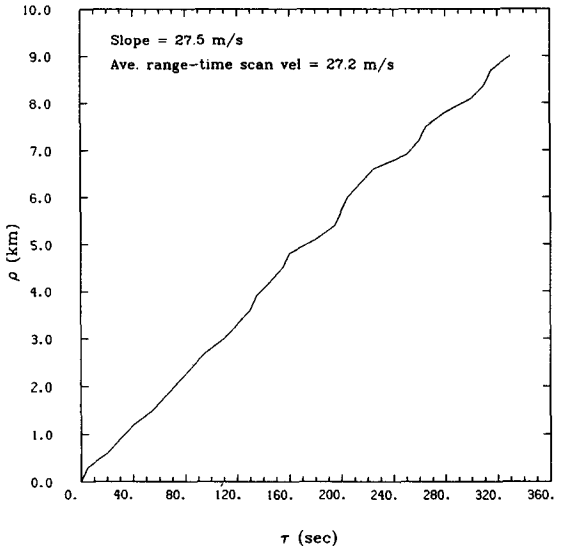

FIG. 17. The primary correlation maximum in Fig. 15 as a function of τ and ρ.

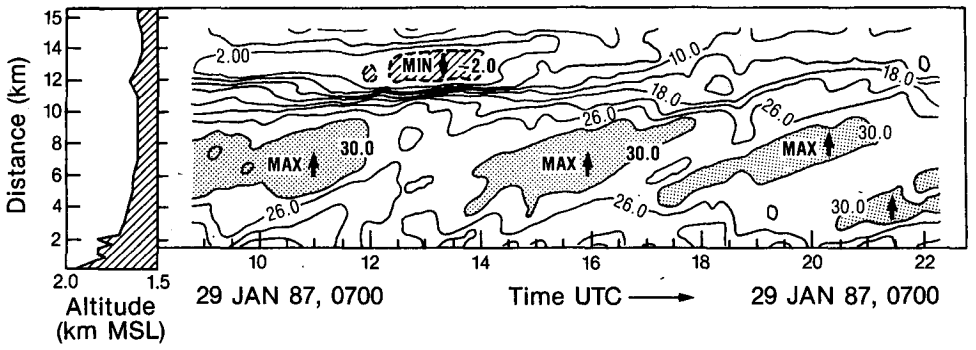

FIG. 18. Range–time display of lidar-measured radial velocities (m s^{-1}) during the period 0708 to 0722 UTC 29 January 1987. The lidar was pointed eastward with an elevation angle of 0°. The optical beam never intersected the ground. The data within this scan were subjected to median and Lanczos filters for display purposes only. Terrain along the lidar beam is shown to the left of the contoured lidar data.

wind gradient is clearly depicted in the 0712:49 UTC 29 January lidar beam scan (Fig. 19). Hoover Hill apparently was not responsible for the flow reversal, despite its coincidence with the location of the wind feature, because the reversal was also documented north of the terrain feature by a three-dimensional lidar scan. Thus, it is suggested that the eastern edge of the mountain wave extended to ~12 km east of the lidar. This may in fact be a hydraulic jumplike feature at the eastern edge of the mountain wave. Durran's (1986) nonlinear, nonhydrostatic windstorm model simulated a hydraulic jump feature in the lee of the mountains in a location similar to that observed by the lidar in the second range–time scan. The PROFS mesonet pressure tendency and maximum wind gusts during the windstorm event (Fig. 20) showed significant pressure falls and strongest gusts confined to the sites close to the Front Range, thus producing further evidence exhibiting the eastern limit of the mountain wave.

Brisk westerly winds approaching 20 m s^{-1} reappeared in the range–time scan ~3 km east of the flow reversal at 12 km. Strong west to northwest winds and prolonged pressure rises were observed by the PROFS mesonet sites in eastern Colorado at this time (Fig. 20). The strong winds in this region were probably synoptic in scale caused by the large-scale west–east pressure gradient that translated eastward from western Colorado (shown in Fig. 4). Time-to-space conversions of the mesonet pressure time series suggested the presence of a significant west–east pressure gradient over eastern Colorado.

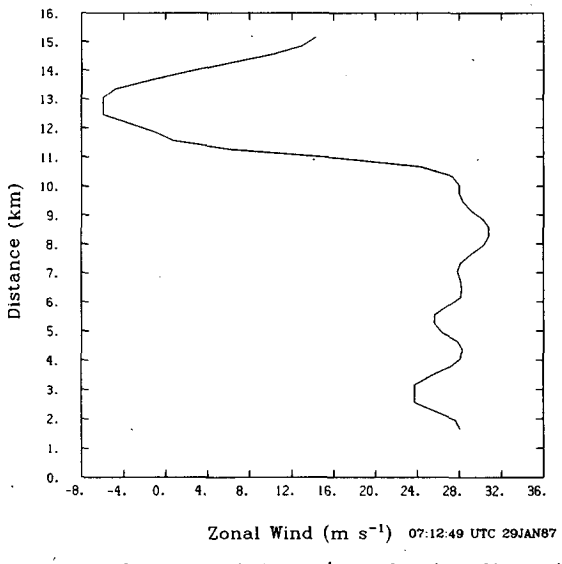

FIG. 19. Plot of the zonal wind (m s^{-1}) as a function of increasing distance east from the lidar at 0712:49 UTC 29 January 1987.

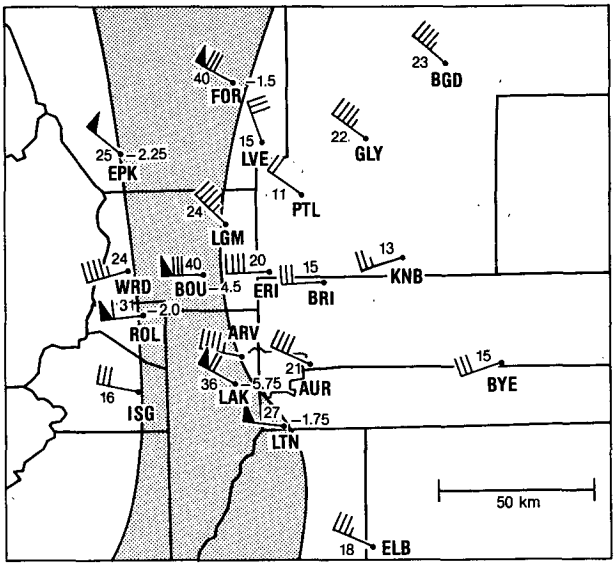

FIG. 20. The PROFS mesonetwork showing the maximum wind gust (m s^{-1}, left portion of station plots) and pressure tendency (mb, right portion of station plots), if any, associated with the windstorm. Wind vectors are as described in Fig. 3. Stippled area is location of mountain wave.

5. Summary

Until last winter, numerical model simulations, with their high spatial and temporal resolution output, have outstripped the ability to observe windstorms. The Doppler lidar is able to observe high-resolution spatial and temporal features that can be compared with the models. The lidar VAD and RHI scans allowed observations of the structure of the lower troposphere in the lee of the Continental Divide during a downslope windstorm, and contained more detail than in-situ and remote sensing observations of previous windstorms. The onset, peak, and decay of the 29 January windstorm in the lowest 2 km were well documented by the VAD/RHI-derived time–height analysis and were supported by supplemental data. The analyzed lower tropospheric leeside wind maximum observed during this windstorm was the first direct documentation of this leeside feature. The unique high resolution capabilities of the lidar allowed detailed observations of propagating wind gusts during the event. These gusts exhibited two distinct periodicities and were apparently advected by the mean wind. Finally, the lidar documented a hydraulic jumplike feature at the eastern edge of the mountain wave east of Boulder.

During the windstorm, three-dimensional lidar scans were also produced, with the lidar beam pointing east from the site. In the near future, these scans will be analyzed to determine the cross-wind or north–south extent of the propagating wind gusts as well as the vertical tilt, if any, of these gusts. The north–south and vertical dimensions of the jumplike flow reversal east of Boulder will also be investigated.

Plans also include model simulations from this data set using either an upstream sounding (possibly Grand Junction) or a vertical slice of the cross section in Fig. 8. Such an exercise may result in new insights into downslope windstorm structure and the analysis of mountain wave dynamics.

During January and February 1989, we intend to utilize again the WPL Doppler lidar for monitoring downslope windstorms. During at least part of this experiment, the lidar will be placed on the High Plains east of Boulder in order to look westward toward and over the foothills. From these data, it is hoped that the source of the wind gusts can be located. The three-dimensional structure of the source region of the gusts, as well as the actual gusts, could also potentially be documented.

Acknowledgments. The contributions of Ronald Richter and Bonnie Weber of NOAA/WPL to this study are recognized and greatly appreciated. Terry Clark of NCAR and John Brown of NOAA/WRP provided helpful discussions and comments related to this work. Time donated by Boba Stankov of NOAA/WPL to generate several graphic displays is greatly appreciated. Significant contributions by Doug Lilly and one anonymous reviewer provided valuable insight into the science presented within the text.

REFERENCES

Brinkman, W. A. R., 1974: Strong downslope winds at Boulder, Colorado. *Mon. Wea. Rev.*, **102,** 592–602.

Browning, K. A., and R. Wexler, 1968: The determination of kinematic properties of a wind field using Doppler radar. *J. Appl. Meteor.*, **7,** 105–113.

Clark, T. L., and R. D. Farley, 1984: Severe downslope windstorm calculations in two and three spatial dimensions using anelastic interactive grid nesting: A possible mechanism for gustiness. *J. Atmos. Sci.*, **41,** 329–350.

Durran, D. R., 1986: Another look at downslope windstorms. Part I: The development of analogs to supercritical flow in an infinitely deep, continuously stratified fluid. *J. Atmos. Sci.*, **43,** 2527–2543.

——, and J. B. Klemp, 1983: A compressible model for the simulation of moist mountain waves. *Mon. Wea. Rev.*, **111,** 2341–2361.

Hardesty, R. M., T. R. Lawrence, R. A. Richter, M. J. Post, F. F. Hall, Jr. and R. M. Huffaker, 1983: Ground-based coherent lidar measurement of tropospheric and stratospheric parameters. *Proc. Soc. Photo-Opt. Instrum. Eng.*, **415,** 85–91.

Klemp, J. B., and D. K. Lilly, 1975: The dynamics of wave-induced downslope winds. *J. Atmos. Sci.*, **32,** 320–339.

——, and ——, 1978: Numerical simulation of hydrostatic mountain waves. *J. Atmos. Sci.*, **35,** 78–107.

Lanczos, C., 1956: *Applied Analysis.* Prentice-Hall, 539 pp.

Lawrence, R. S., G. R. Ochs and S. F. Clifford, 1972: Use of scintillations to measure average wind across a light beam. *Appl. Optics,* **11,** 239–243.

Lilly, D. K., and E. J. Zipser, 1972: The Front Range windstorm of 11 January 1972: A meteorological narrative. *Weatherwise,* **25,** 56–63.

Peltier, W. R., and T. L. Clark, 1979: The evolution and stability of finite-amplitude mountain waves. Part II: Surface wave drag and severe downslope windstorms. *J. Atmos. Sci.*, **36,** 1498–1529.

Post, M. J., R. L. Schwiesow, R. E. Cupp, D. A. Haugen and J. T. Newman, 1978: Temporal and spatial frequency spectra for atmospheric aerosols. *J. Appl. Meteor.*, **17,** 1179–1181.

——, R. A. Richter, R. M. Hardesty, T. R. Lawrence and F. F. Hall, Jr., 1981: National Oceanic and Atmospheric Administration's (NOAA) pulsed, coherent, infrared Doppler lidar—Characteristics and data. *Proc. SPIE,* **300,** 60–65.

Pratte, J. F., and L. Kaimal, 1986: *Surface Mesonetwork Operator's Manual,* 2nd version. [NOAA/ERL Program for Regional Observing and Forecasting Services (PROFS), Boulder, Colorado, 80303.]

Rothermel, J., C. Kessinger and D. L. Davis, 1985: Dual-Doppler lidar measurement of winds in the JAWS experiment. *J. Atmos. Oceanic Technol.*, **2,** 138–147.

Vellerman, P. F., and D. C. Hoaglin, 1981: *Applications, Basics, and Computing of Exploratory Data Analysis.* Duxbury Press, 354 pp.